Stability and stoichiometry of (polar) oxide surfaces for varying oxygen chemical potential

2008 J. Phys.: Condens. Matter 20 184014

(http://iopscience.iop.org/0953-8984/20/18/184014)

J. Phys.: Condens. Matter **20** (2008) 184014 (13pp) doi:10.1088/0953-8984/20/18/184014

Stability and stoichiometry of (polar) oxide surfaces for varying oxygen chemical potential

A Barbier[1], **A Stierle**[2], **F Finocchi**[3] **and J Jupille**[3]

[1] CEA-Saclay, DSM/DRECAM/SPCSI, 91191 Gif-Sur-Yvette, France
[2] Max-Planck-Institut für Metallforschung, Heisenbergstraße 3, D-70569 Stuttgart, Germany
[3] INSP, Université Pierre et Marie Curie-Paris 6, CNRS, UMR 7588 Campus Boucicaut, 140 rue de Lourmel, 75015 Paris, France

Received 3 August 2007, in final form 18 September 2007
Published 17 April 2008
Online at stacks.iop.org/JPhysCM/20/184014

Abstract
Polar oxide surfaces constitute a class of surfaces long considered as unstable because of their theoretically predicted diverging electrostatic surface potential, although such crystal orientations form spontaneously in nature. Because of the intrinsic hindrances (charge build-up, electron correlation effects) a reliable description of such surfaces necessitates a combined theory–experiment approach. Experimentally, detailed investigations became possible in recent years because of the availability of charge build-up insensitive techniques such as surface x-ray diffraction, which is thoroughly used in the presented work. We consider here prototypical polar oxide surfaces of different crystalline structures and show that their stability regime strongly depends on the external conditions applied to the surface in terms of oxygen chemical potential. In order to understand the structure and stability of polar oxide surfaces, their chemical environment must be included.

(Some figures in this article are in colour only in the electronic version)

1. Introduction

The surface composition and structure of a multi-component material is a fundamental property that has tremendous consequences for its surface reactivity. Within real conditions, as far as oxide compounds are concerned, the oxygen chemical potential plays a crucial role since oxygen is both a major component of oxide materials and a reactive species in the environment. Generally speaking, examination at near-normal pressure conditions demonstrates that the extreme surface can dramatically affect the macroscopic properties of a substrate. Under a water partial pressure close to 1 mbar at 295 K, photoemission measurements show that the behaviour of the Cu(111) surface, which is not wetted at all by water, contrasts with that of Cu(110), which is covered by a mixture of OH and H_2O. But, on O-precovered Cu(111), the same OH and H_2O mixture appears [1]. The adsorption behaviour on Cu(111) can therefore be controlled by a tiny modification of the surface. On Pt(110), the presence of surface oxide strongly enhances the rate of the CO (carbon monoxide) oxidation reaction with respect to the bulk-terminated Pt surface [2, 3]. When exposed to a partial pressure of a few tenths of a mbar, a Pd cluster supported on TiO_2 reversibly switches from truncated tetrahedra under hydrogen to close to spherical when exposed to oxygen [4]. These examples demonstrate that a few surface atoms can act as a joystick that determines the exchange of the bulk with the surrounding atmosphere. As for oxide surfaces, which are the topic of interest herein, the surrounding pressure, acting as the key parameter, has long been neglected and many samples have been investigated in ultra-high vacuum (UHV) conditions, resulting in misleading conclusions when extrapolated to the surface reactivity in real conditions.

This is particularly true for polar oxide surfaces. They were long believed to be unstable, according to early experimental evidence of (100) faceting on MgO(111) [5] and to Tasker's [6] classification, which predicts a diverging surface energy for terminations showing a net dipole moment perpendicular to the surface. However, such surfaces spontaneously form in environmental conditions and many crystals are daily used in laboratories. Polar oxide terminations are encountered in a number of crystallographic structures, including rock-salt, corundum, spinel, inverse spinel, wurtzite and perovskite, which were reviewed by Noguera [7, 8].

A puzzling case to illustrate the stability of a polar termination is that of the ZnO crystal in a basal orientation, which shows simultaneously the two polar orientations, (0001)-Zn on one side and $(000\bar{1})$-Zn on the other side. In addition, these orientations resist the etching in different manners which can be used to distinguish them [9]. However, polarity can be cured by a charge compensation which often takes place at the very surface of the crystal and only involves a fraction of an atomic monolayer. It arises through three different mechanisms: (i) a change in composition of surface layers, (ii) a chemisorption of foreign atoms or ions, (iii) a charge redistribution over the surface layers [7]. The former is very common. It is expected to occur at the surface of the corundum (0001) face on which the termination by a single metal layer M results in a M–O_3–M repeat unit with zero dipolar moment [7]. It has been observed by x-ray diffraction on a bulk α-Al_2O_3(0001) [10] and on the ZnO(0001)–Zn surface which polarity is suggested to be cured by a removal of Zn atoms either at random [11] or at the steps of triangular shaped islands [12]. In a similar manner, the $(\sqrt{2} \times \sqrt{2})$R45° surface reconstruction of magnetite (Fe_3O_4), which crystallizes in the inverse spinel structure, is associated with a termination by either a half-filled layer of Fe^{3+} [13], or a layer of oxygen anions with one oxygen vacancy per unit cell [13, 14] on which a Jahn–Teller distortion is predicted [15]. The alternative solution—the adsorption of one hydroxyl group per unit cell on the surface oxygen atoms [13]—clearly belongs to the second category of mechanisms, as well as the prediction of the stabilization of MgO(111) by a hydroxyl adlayer in wet conditions [16]. The third case is encountered on MgO(111) in oxygen-poor conditions, for which polarity is compensated for by the appearance of almost neutral surface Mg atoms [17]. This mechanism is also suggested in the case of the polar ZnO surfaces [18].

The inclusion of the oxygen chemical potential in calculations is therefore mandatory. The existence of phase diagrams in experimental data (case of hematite α-Fe_2O_3(0001) [19, 20] and more theoretically for alumina α-Al_2O_3 (0001) [21]), or at least of phases which can only exist if stabilized by an appropriate chemical potential (magnetite Fe_3O_4(001) [13, 15]), requires a comparison with theory. Neglecting such an approach leads to an oversimplified octopolar reconstruction scheme [22] in the case of rock-salt ionic surfaces. The problem becomes even more difficult when strong d–d correlation effects have to be taken into account. Strong electron correlation effects, not included in a density functional description, were described by a Hubbard-type on-site Coulomb repulsion (DFT + U approach). The value of the U potential is typically determined in order to provide an agreement with the chosen bulk experimental parameters. Its value may have tremendous effects on the determination of the stable surface termination [23] and the electronic character of the gap [24]. More importantly the bulk refined value of U may not remain valid in the surface region.

Many studies on oxide surfaces are performed on supported thin films because such samples allow investigations by scanning tunnelling microscopy without any charging problem. Drawbacks are that the experimental observations are often mingled with interpretations due to the fact that, for example, (i) thin films can hardly be assumed to mimic bulk materials and (ii) the use of surface preparation concepts works well for metals and semiconductors but does not consider the severe modifications they induce on oxide surfaces. A second difficulty is specific to environmental approaches. Many surface probes are not compatible with elevated pressures (temperatures) and measurements can only be performed in vacuum (at room temperature). Surface x-ray diffraction (SXRD) experiments, which are methods of choice to study insulators, have proven not to suffer from the above drawbacks and to be suited to investigating the surface structures and relaxations of oxide surfaces in any conditions [15, 17, 25–27]. As a general rule, for crystals of high-crystalline quality, diffraction experiments provide direct observations on the space groups and periodicities. On the contrary, the experimental lattice content, i.e. the motif, remains an interpretation. The actual motif necessarily reproduces the experimental structure factors but a good match with data is not enough to validate the structural model. Unfortunately, bulk oxides are often good insulators, preventing cross checking by additional experimental approaches.

In the present paper, x-ray diffraction data and theory are used to cross check each other in order to derive the best possible structural model which also makes sense from the first principle approach. We will discuss two important classes of structures that have polar surfaces and provide prototypical materials exhibiting strong or weak electronic correlation effects, namely rock-salt ionic oxides and hematite.

2. Methods

2.1. Surface x-ray diffraction

For a half-infinite system, as represented by a single crystal with a well prepared surface, the reciprocal lattice is intrinsically surface sensitive by the truncation of the crystal. The Bragg reflections are interlinked by structure factor rods (so-called crystal truncation rods (CTR)), which run perpendicular to the surface of the crystal. Any additional periodicity on the surface gives rise to surface rods, which contain information on the structure of the reconstructed layer only. Surface x-ray diffraction is now a well established technique and several review papers are available describing in detail the technique; the interested reader may refer to them [27–30].

Besides the possibility of determining surface structures with very high accuracy (typically ±0.01 Å in atom position), SXRD has other great advantages, directly linked to the photon-in–photon-out nature of the technique. It is by essence charge build-up insensitive and thanks to beryllium windows, which are transparent to hard x-rays, variable sample environments can be used. Recently several setups have been developed that enable the study of surfaces from the UHV regime up to high pressures (up to 2 bars) at elevated temperatures (typically 1200 K) [31, 32]. The works discussed hereafter largely benefited from these developments.

SXRD suffers also some drawbacks. Since the scattering arising from the surface region is about six orders of

magnitude smaller than the bulk one, synchrotron radiation and single crystals of very high structural quality are mandatory. Moreover, the Thompson scattering is roughly proportional to the square of the atomic number, making the technique less sensitive to light elements. Because of the phase information loss, the knowledge of the motif within the unit cell is derived from relative intensities of diffraction peaks on the basis of a structural model obtained through a strongly nonlinear trial/error fitting procedure.

Surface x-ray diffraction provides a measurement of the reciprocal space, and hence structure factors, in three dimensions. By convention, the H and K indexes describe the in-plane momentum transfer (in reciprocal lattice units, r.l.u., of the single crystalline surface) and L the perpendicular momentum transfer.

2.2. Thermodynamical aspects

Thermodynamics describes the equilibrium properties of matter as a function of external macroscopic parameters. When describing oxide surfaces three regions have to be defined: (i) the bulk oxide, (ii) a large gas phase region consisting of molecular oxygen at pressure p_{O_2} and (iii) a surface region (in contact with a bulk reservoir for the oxide and the gas phase, both under chemical potentials μ_{ME} and μ_{O_2}) with *a priori* unknown chemical composition, stoichiometry and structure. The entire system is surrounded by a thermal bath of temperature T. The adequate thermodynamic potential is in this case the Gibbs free energy $G(T, p, N)$, p denoting the pressure and N the number of atoms. The surface free energy γ is defined as

$$\gamma(T, p) = \frac{1}{A}(G(T, p, N_{ME}, N_O) - N_{ME}\mu_{ME}(T, p) - N_{ME}\mu_O(T, p)) \quad (1)$$

γ represents the Gibbs free energy difference between a crystal including a given surface and the same crystal with bulk termination, normalized to the surface area A. The most stable surface composition minimizes γ. The metal (ME) and oxygen (O) chemical potentials are interlinked by the composition of the bulk material, serving as a reservoir for ME atoms. For a bulk formula ME_xO_y one obtains:

$$x\mu_{ME} + y\mu_O = \mu^{bulk}_{ME_xO_y}. \quad (2)$$

In the first approximation (mostly valid for many systems) the Gibbs free energy can be directly expressed by the internal energy E. In general the Gibbs free energy can be written as:

$$G = E + PV - TS. \quad (3)$$

The PV term can be neglected compared to the surface energy for the pressures under consideration here, as well as the TS term, including entropy contributions. The internal energy E is equal to the total energy $E^{total}(N_{ME}, N_O, V)$, if one neglects the vibrational contribution to E. $E^{total}(N_{ME}, N_O, V)$ is the quantity accessible by density functional theory (DFT) calculations.

For a symmetric DFT slab the following result is obtained for γ:

$$\gamma = \frac{1}{2A}\left(E^{total}_{slab} - \frac{1}{x}N_{ME}\mu^{bulk}_{ME_xO_y} + \left(\frac{y}{x}N_{ME} - N_O\right)\mu_O\right). \quad (4)$$

Here N_{ME} and N_O denote the number of metal and oxygen atoms inside the slab.

Assuming conditions in which intermolecular interactions can be neglected and considering the molecular oxygen bath as an ideal gas, one can express the chemical potential of oxygen, μ_{O2}, as a function of temperature, T, and oxygen partial pressure p_{O2} as:

$$\mu_O(T, p_{O2}) = \mu_{O2}(T, p^0) + \frac{1}{2}kT\ln\left(\frac{p_{O2}}{p^0}\right). \quad (5)$$

The oxygen chemical potential is frequently referenced at $T = 0$, $p = 0$ to one half of the total energy of the oxygen molecule $\mu_O(T = 0, p = 0) = \frac{1}{2}E^{total}_{O2}$.

In surface energy diagrams, γ is plotted as a function of $\Delta\mu' = \mu(T, p_{O2}) - \mu(T = 0, p = 0)$. γ exhibits according to equation (4) a linear behaviour in μ'. A reference structure can be found for which the third term in equation (4) is 0, yielding a surface free energy independent of μ'. For structures with excess oxygen at the surface with respect to this reference structure, a negative slope will be found in the $\gamma(\Delta\mu)$ diagram and vice versa, for oxygen deficient structures a positive slope is expected for $\gamma(\Delta\mu)$. In both cases the slope is given by the deviation from the stoichiometry of the reference structure.

At a given temperature and pressure, the thermodynamically most stable system minimizes its surface free energy by establishing thermal equilibrium with the gas phase. It is thus expected that the relative amount of cations and anions changes in the surface region with respect to the oxygen chemical potential. The μ_{O2} range of interest is limited by the conditions that the oxide material does not decompose (leading to metallization) or transform into other bulk oxide phases and that molecular oxygen does not condense on the surface. However, theory requires the input of structural configurations, before structural optimization, for which the Gibbs free energy will be minimized, limiting the predictions to the investigated surface configurations.

3. Environment dependent structural stability

3.1. Rock-salt(111) surfaces

Changes in environment, in particular changes in chemical potential of oxygen, may create appropriate conditions for a stabilization, as exemplified by the occurrence of the MgO(111) orientation in a variety of conditions. When annealed in vacuum, MgO(111) proves to be unstable towards a macroscopic reorganization into (100) [5] or vicinal (111) [33] facets. At variance, a treatment at 1850 K in air leads to a p(2 × 2) reconstruction, which stabilizes the polar orientation [17]. Upon dissolution in water, the common MgO smoke crystallites—cubic with (100) faces—are seen to become octahedra limited by (111) facets [34], in agreement with theoretical calculations which predict that the hydroxylated MgO(111) surface is the orientation of lowest energy in wet environment and should dominate MgO in

Table 1. Schematic drawing of different rock-salt (111) terminations terminated by either oxygen or metal (ME) atoms. Large circles stand for oxygen and small ones for metal atoms. The ME-oct configuration is similar to the O-oct one considering a simple anion and cation exchange.

	O-Spinel	**ME**-hex	**O**-Oct
	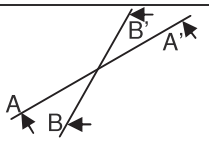	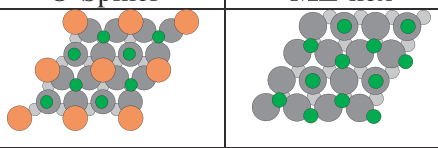	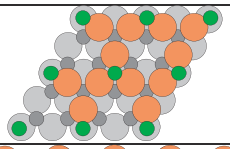
A-A’	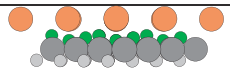	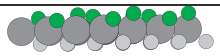	
B-B’	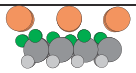	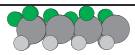	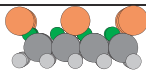

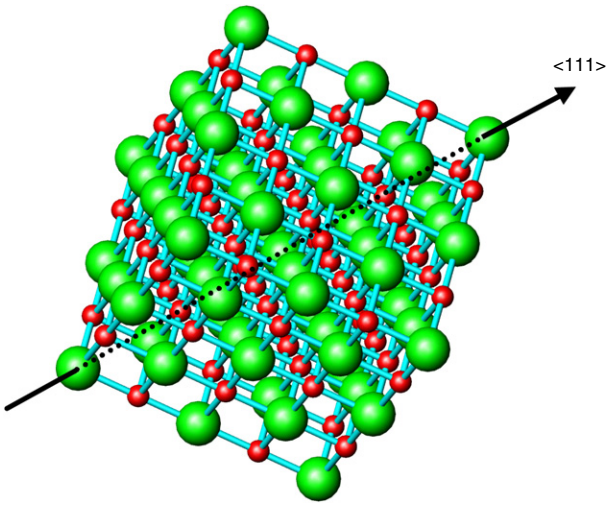

Figure 1. Schematic drawing of the Na–Cl rock-salt crystalline structure highlighting the stacking of alternating cationic and anionic sheets along the ⟨111⟩ direction. Anions are represented by large atoms and cations by small ones.

‘normal’ conditions [16]. Surroundings can also shift a polar orientation from one mode of compensation to another. Internal oxidation of Cu–Mg alloys leads to the formation of MgO crystallites with (111) facets which, for high values of the chemical potential of oxygen, are O-terminated with interfacial copper in a Cu_2O-like state. However, in oxygen-poor conditions, the interface consists of metallic copper and oxygen deficient magnesia [35–37].

Such behaviour might be the reason why stabilization of rock-salt ionic metal-oxide (111) surfaces has puzzled surface scientists over decades. The issue is linked to the classical Madelung problem, i.e. the divergence of the Coulomb potential occurring for ionic crystal surfaces. Rock-salt ionic crystals (space group $Fm\bar{3}m$, O_h^5, no.225 [38]) consist of a stacking of alternating cationic and anionic sheets along the ⟨111⟩ direction as pictured in figure 1. Without surface reconstructions or charge redistribution, the surface planes carry a net dipolar moment. This class of surfaces (type I in Tasker classification [6]) can thus be considered as one of the simplest structure that has to overcome the diverging Coulomb potential of polar oxide surfaces since the simple truncated surfaces have a divergent electrostatic energy, in theory making them highly unstable [6]. However, the technological importance in catalysis [39] and magnetoresistive sensors [40, 41] of polar oxide surfaces revived the interest in the topic.

Separate experimental and theoretical works failed in describing this class of surfaces. Rock-salt ionic metal-oxide bulk materials are generally good insulators. The use of metal-oxide thin films, grown on metal substrates, can more easily be studied. Unfortunately, they may exhibit very different surface terminations and/or configurations even within the same reconstruction unit mesh as could clearly be evidenced for NiO(111) [25].

Considering the polar (111) orientation of the metal-oxide series of rock-salt compounds, the following experimental facts should be kept in mind: (i) when thermodynamically allowed the (111) termination is overruled by more stable phases (e.g. different surface stoichiometries) at the surface (case of CoO(111) and MnO(111) [10]); (ii) decomposition and metallization occur when they are annealed in an oxygen-poor environment [42]; (iii) their stabilization by reconstructions—mainly p(2 × 2), as for NiO [25, 43] and MgO [44]—suggests the coexistence of several motifs depending on the oxygen potential and preparation conditions (by deposition of thin films or by cutting and polishing single crystals) [25, 45].

NiO(111) is by far the most stable metal-oxide of the series and can be prepared with a very good surface crystalline structure [25, 46, 47] which is clearly p(2 × 2) reconstructed. Exposing this surface to increasing temperatures under moderate oxygen partial pressures (typically 10^{-6} mbar) does not modify the reconstruction mesh but leads to obvious rearrangements in the motif. This is best illustrated by considering the self-correlation (or Patterson) maps (figure 2) derived from in-surface-plane reconstruction peaks. A well pronounced hexagonal-like mesh develops progressively upon annealing. In a first interpretation attempt, these maps could successfully be reproduced using a combination of two surface reconstructions consisting of (i) a Ni-terminated octopolar reconstruction (noted Ni-oct) and (ii) an oxygen-terminated spinel-like configuration (noted O-spi) as could be expected from a Ni_3O_4 layer, which is thermodynamically unfavourable in the bulk [25, 47] (see table 1 for real

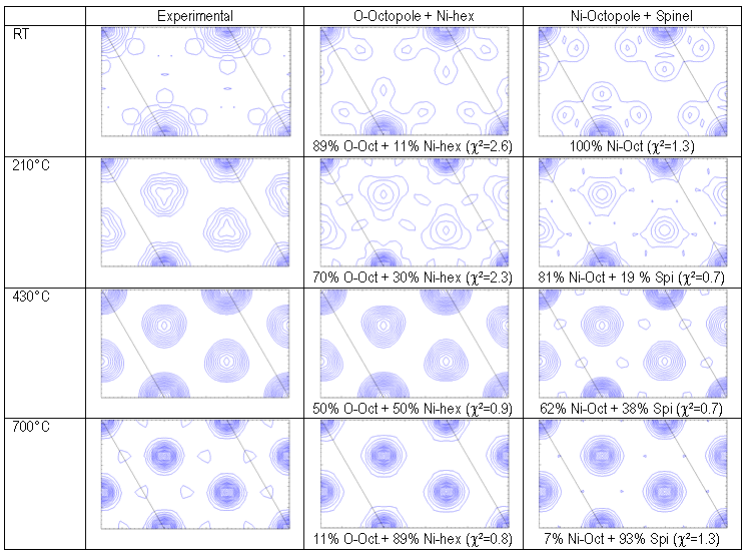

Figure 2. Experimental and calculated self-correlation (Patterson) maps measured on NiO(111) surfaces at the temperatures indicated in the left column. The second column contains the experimental maps, the third the best decomposition assuming a combination of O-terminated octopoles and epitaxial hexagonal Ni atoms, the last column contains the best decomposition assuming a combination of Ni-terminated octopoles and spinel configurations. The experimental data were measured at the critical angle for total external reflection of the x-rays (beamlines BM32 (18 keV incident energy) and ID03 (17 keV incident energy) at the ESRF (Grenoble, France)).

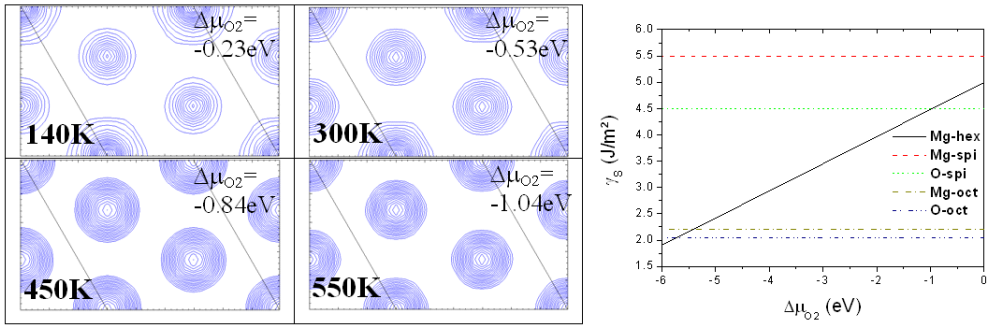

Figure 3. Left: experimental self-correlation (Patterson) maps measured on MgO(111) at the temperatures indicated in the figure. The surface was always exposed to a partial pressure of oxygen of about 10^{-6} mbar. The experimental data were measured at the critical angle for total external reflection of the x-rays (beamline ID03 (17 keV incident energy) at ESRF). Right: calculated surface energy for various MgO(111) surface terminations with respect to the chemical potential of oxygen.

space drawings). Unfortunately NiO belongs to the strongly correlated class of materials, preventing reliable theoretical calculations. The successful preparation method developed for NiO single crystals could be transposed to MgO(111) and experiments could be performed without surface decomposition or reduction [17]. Since the diffracted intensity is to the first order proportional to the squared atomic number, the scattering arising from MgO is expected to be half an order of magnitude smaller than the one measured on NiO. Single crystals of very high quality were thus required and obtained [17]. Within a different range of oxygen chemical potentials, the self-correlation maps measured for MgO(111) show great similarities with those measured on NiO(111) (figure 3). Moreover the structural model that reproduces the NiO(111) surface diffraction data (O-spinel + Ni-octopole) also reproduces the in-surface-plane and out-of-surface-plane SXRD data measured on MgO(111). However, the transition between both configurations would require a complex interlayer atomic diffusion, a puzzling behaviour when considering that it occurs close to room temperature and remains active down to 140 K for MgO(111). Hence, although the SXRD model (O-spinel + metal-octopole) successfully reproduces all data sets for MgO(111) and NiO(111), it remains unsatisfactory since it involves unusual atomic configurations and is hardly of any help to explain the experimentally observed reversibility which occurs upon simple air-exposure at room temperature.

Fortunately, MgO(111) is a simple ionic material for which theoretical approaches should be valid. Density functional theory calculations were carried out by using pseudopotential plane-wave techniques [48], in the framework of the generalized-gradient approximation (GGA) [49] to the exchange and correlation energy. The norm-conserving pseudo-potentials were extensively tested [50]. Up to nine

Table 2. DFT-GGA calculated energy gap, surface energy (γ) and residual surface stress in the GGA slab (σ) as a function of MgO surface configurations.

	p(2 × 2) O-oct	p(2 × 2) Mg–oct	p(2 × 2) O-spinel	p(2 × 2) Mg-spinel	(1 × 1)	Mg-hex $\Delta\mu(O_2) = 0$ eV	Mg-hex $\Delta\mu(O_2) = -6$ eV
Gap (eV)	2.9	2.2	0.7	~ 0	0	1.65	1.65
γ (J m^{-2})	2.05	2.2	4.5	5.5	5.6	5	1.9
σ (meV Å^{-3})	−5	−7.5	+4.6	+1		−0.1	−0.1

Table 3. Mg-oct, O-spi, O-oct, Mg-hex configurations. The computed atomic positions in the outermost layers are given in units of the lattice vectors $\mathbf{a_1} = a\sqrt{2}(1; 0; 0)$, $\mathbf{a_2} = a\sqrt{2}(-1/2; \sqrt{3}/2; 0)$ apart from the third component, which represents the relative relaxation along the [111] direction with respect to the ideal stacking $a/2\sqrt{3}$. Lower part: optimal ratios for the different structures as derived from the SXRD data at 300 and 550 K. χ^2 is computed from the in-plane SXRD data.

	Mg–oct	O-spi	O-oct	Mg-hex
x, y, z	1/3, 2/3; −6.4% (Mg)	2/3, 1/3; +16% (O)	1/3, 2/3; −4.0% (O)	
	0.9910, 0.5094; −1.6% (O)	2/3, 1/3; +6.8% (Mg)	0.9655, 0.5173; −3% (Mg)	2/3, 1/3; +8.5% (Mg)
	0.4905, 0.5094; −1.6% (O)	0, 0; −1.3% (Mg)	0.4827, 0.5173; −3% (Mg)	0, 0; −2.0% (Mg)
	0.4905, 0.9910; −1.6% (O)	1/3, 2/3; −3.2% (Mg)	0.4827, 0.9655; −3% (Mg)	1/3, 2/3; −4.3% (Mg)
	2/3, 1/3; +12.8% (Mg)	2/3, 1/3; −12.6% (O)	2/3, 1/3; +22.1% (O)	2/3, 1/3; −5.2% (O)
	0.6481, 0.824; −2.5% (Mg)	0.6685, 0.8347; −0.1% (O)	0.6582, 0.8291; −3.8% (O)	0.6694, 0.8347; +2.8% (O)
	Model Mg-octopole + O-spinel		Model O-octopole + Mg-hex	
300 K	33% + 67%		46% + 54%	
550 K	0% + 100%		13% + 87%	

special k-points were used to sample the irreducible Brillouin zone. The various p(2 × 2) surfaces were simulated through slabs for which any laterally averaged quantity $\bar{f}(z)$ is symmetric under inversion, and thick enough to reduce the error bar on the computed surface energy and stress below 0.1 J m^{-2}. The geometry optimization is considered to be achieved when the maximum force on the atoms does not exceed 10 meV Å^{-1}. Although, the DFT calculations performed at 0 K for MgO predict a spinel-like configuration that corresponds to a local minimum in energy, it turns out to be unstable against small atomic displacements and its surface energy is much higher than that of the octopole (table 2). The model including surface ozone [44] could also be discarded. It reproduces poorly the experimental data and the calculations show that it is unstable with respect to the unreconstructed (1 × 1) surface.

A subsequent tentative interpretation of the evolution of the in-plane SXRD data by means of a competition between the two terminations (Mg-oct and O-oct) of the octopole reconstruction was unfruitful. Indeed, the in-plane self-correlation map recorded at high temperature (HT) and low p_{O2} indicates strongly inequivalent subsurface cations which cannot be accounted for by the octopole structures that, accordingly, do not fit the SXRD data.

Models for which the stoichiometry was set in order to heal the polarity with formal charges are unable to represent the experimental data. By analogy with other oxide surfaces, showing decomposition and/or metallization in reducing conditions, a (0001) oriented epitaxial Mg layer (hereafter noted as Mg-hex) was considered. Its optimized geometry is given in table 3. Indeed, its surface energy has a linear behaviour as a function of $\Delta\mu_{O2}$ (figure 3-right), from 5.0 J m^{-2} ($\Delta\mu_{O2} = 0$) to 1.9 J m^{-2} at the lower limit ($\Delta\mu_{O2} = -6.1$ eV). (The excess oxygen chemical potential $\Delta\mu_{O2} = \mu_0 - \mu_{O2(gas)}$ is negative and its lower limit is given by the formation energy of MgO(solid) with respect to O_2(gas) + Mg(solid).) We note that the lower limit of $\Delta\mu_{O2}$ is very small in the case of MgO, indicating that the dissociation of the Mg–O molecule requires very low potentials and is thus unlikely. Upon annealing, the Mg–O molecule is evaporated rather than dissociated which is consistent with experimental observations [5]. From the DFT calculations the stability region of Mg-hex corresponds to very small $\Delta\mu_{O2}$ values (i.e. very small oxygen partial pressures and high temperatures) whereas a large fraction is necessary to reproduce the room temperature SXRD data. As a matter of fact the DFT calculations do not address the optimization of the mixture of terminations and additional considerations, such as the release of the surface stress achieved by combining O-oct and Mg-hex, cannot be taken into account although it may shift the stability domain of Mg-hex (within a mixture) to larger $\Delta\mu_{O2}$ values. Such an approach would require further theoretical work.

Mg-hex is a rare example of polarity compensation through the anomalous filling of surface states [51]. Nevertheless, it turns out to be insulating, with a DFT HOMO–LUMO (highest occupied molecular orbital energy–lowest unoccupied molecular orbital energy) gap of the same order as the O-oct. The analysis of the computed topological charges [52] of the inequivalent surface atoms shows that the one-fold coordinated Mg(1) is almost neutral, consistent with the weak Madelung potential exerted by the neighbouring charges. The HOMO has a dominant Mg(1) character and corresponds to a gap state located slightly above the top of the MgO valence band.

A weighted mixture of (O-Oct + Mg-hex) allows a very good reproduction of the diffraction data as well as the (Mg-Oct + O-spi) derived from the NiO(111) data analysis.

We can now build a (O-Oct + Ni-hex) model by analogy and revisit the NiO(111) data. As a matter of fact very good data reproductions are possible, although with different relative weights (figure 2) as compared to the spinel model. We note also that the χ^2 agreement factor value is hardly of any help here to discriminate between both models. The present study is a typical example of a non-unique solution for the x-ray data, since the structure factors for both models are almost equivalent. Only the comparison with calculations allowed us to disentangle the situation. Tentatively, the different temperature ranges for MgO and NiO may be linked to the fusion temperature of the corresponding metal (T_f(Mg) $\sim$ 920 K, T_f(Ni) $\sim$ 1730 K) since the full metal-hex termination is obtained at roughly $2T_f/3$. In the case of MgO, Mg sublimation is likely to happen at relatively low temperature and so, in turn, is the sublimation of the Mg–O molecule which has high stability, explaining the strong faceting that is obtained well below the fusion temperature of bulk MgO. NiO annealing at elevated temperatures produces O desorption since metallic Ni islands are formed [42]. Importantly, although of very different nature, within their respective stability domains the polar MgO(111) and NiO(111) surfaces undergo similar structural transformations with respect to $\Delta\mu_{O2}$. The necessary charge compensation phenomenon is not limited to oxide polar surfaces and has been similarly reported for the rock-salt NaCl(111) surface. When grown on Al(111) and Al(100) in vacuum, triangular shaped (111) bulk-terminated islands are formed which experience a charge redistribution of the topmost layers to reach charge neutrality [53]. For NaCl(111) surfaces exposed to water or formamide liquid layers, SXRD experiments combined with AFM observations showed that the polar surface is not reconstructed and charge neutrality is obtained through the presence of a disordered electrochemical double layer with a composition corresponding on average to the p(2 × 2) octopole reconstruction [54].

To summarize, the p(2 × 2) reconstructions of the MgO(111) and NiO(111) surfaces have been understood by combining SXRD experiments with DFT simulations. We found that the low- and high-temperature phases are made of a mixture of distinct configurations with O-octopole and epitaxial metal layers in variable proportions as a function of the oxygen chemical potential. The path between the two phases involves O desorption and surface metal diffusion, which stands in good agreement with the experimentally observed reversibility of the transformations. Although DFT calculations are not possible for NiO(111), the theoretically refined structures obtained for MgO(111) may be applied to NiO(111) as well.

3.2. Hematite(0001)

Iron oxides belong to the most abundant minerals on Earth and occur within a large variety of stoichiometries, structures and properties. They are derived from the corrosion of iron [55] and exhibit the full variety of magnetic properties ranging from antiferromagnetism and canted antiferromagnetism [56, 57] to semimetal ferrimagnetism [15, 58], opening the route to important applications including magnetic storage media and sensors with high sensitivity. Hematite is the most stable phase in the highest oxidation state. Because of its important properties it has been intensively studied over decades [57]. It is a sorbent of toxic metals [59], is involved in toxic gas sensors [60] and hematite clusters were suggested to suppress undesirable greenhouse gases [61]. Genuine properties are expected and/or were evidenced when iron oxides show reduced dimensions, as for example modified sublattice magnetization directions for hematite particles [62].

The α-Fe_2O_3(0001) surface is a model system which has attracted many theoretical and experimental groups, with the unsolved question of the stoichiometry of the surfaces under study. The α-Fe_2O_3(0001) surface is also a test bed for models involving a Hubbard-type on-site Coulomb repulsion (DFT+U approach) to account for strong d–d repulsion [23].

3.2.1. Single crystal surface termination. The hematite group consists of closely related trigonal oxides that share similar structures. The general formula for this group is ME_2O_3 where the ME cations can be either Fe, Ti, Al, Cr, V, Sb, Na and/or Mn. It is isostructural to a wide class of very important oxides including, for example, Cr_2O_3, V_2O_3 and Al_2O_3. Hematite (α-Fe_2O_3) crystallizes in the hexagonal corundum structure (space group $R\bar{3}c$ ($D_{3d}{}^6$, no. 167 [38]) with six formula units with parameters ($a = b = 5.038$ Å, $c = 13.772$ Å) and internal coordinates ($x = 0.3027, z = 0.355\,28$) [63]. The bulk unit cell consists of an alternated stacking, along the c-axis, of two Fe^{3+} planes (12 in the unit cell) with three O^{2-} ions arranged with a three-fold symmetry. No two planes among the 18 of the unit cell are equivalent, under any translation. Cations occupy spaces in layers between the oxygen layers and each is bonded to three oxygen atoms in the above layer and three oxygen atoms in the bottom layer. In order to respect the ME_2O_3 stoichiometry, not all of the sites for these cations are occupied as only two out of three are filled. The bulk structure is pictured in figure 4.

The possible α-Fe_2O_3(0001) surface terminations have attracted a lot of attention both from experimentalists [64–69] and theoreticians [19, 23, 24, 70]. Nevertheless, separately clear conclusions could not be reached. In the present case, even the theoretical predictions disagree. The *ab initio* DFT without [19] or with the GGA [23, 70] predicts that the Fe-terminated surface of hematite is preferred at low oxygen pressures and that O-terminated surfaces should occur at increasing oxygen chemical potentials, leaving a small stability domain to ferryl-terminated surfaces. The inclusion of a Hubbard-type on-site Coulomb repulsion (GGA + U approach) predicts a ferryl-terminated surface at high μ_{O2} and Fe-terminated surfaces at low potentials [23]. In GGA+U, the O-terminated surface is out of the physically meaningful range of $\Delta\mu$.

For thin films produced by atomic oxygen-plasma assisted molecular beam epitaxy, thus in highly oxidizing conditions, a Fe-terminated surface has been reported [67]. In scanning tunnelling microscopy (STM) experiments mixed surfaces were observed: Wang *et al* interpreted their images considering O- and Fe- terminated domains for an oxidized Fe_3O_4 layer

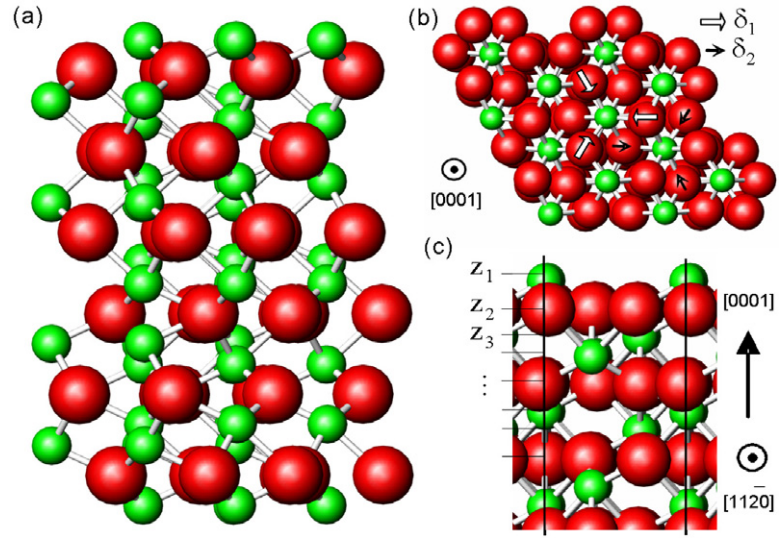

Figure 4. Schematic drawing of the α-Fe_2O_3(0001) structure. Large (small) circles stand for O (Fe) atoms. (a) Bulk structure of a complete out of plane mesh. Top (b) and side (c) views with symmetry elements and allowed relaxations. Radial relaxations of the O atoms are labelled by δ_i and relaxations of layer i along the [0001] axis by z_i.

deposited on Pt(111) [71] whereas Ketteler *et al* suggested the presence of hydroxyl groups by dynamical low energy electron diffraction (LEED) investigations and Lemire *et al* [69] gave evidence of the GGA predicted ferryl groups [23, 70] coexisting with a Fe-terminated surface; Condon *et al* reported FeO(111) [72] and Fe_3O_4(111) [64] domains for sputtered–annealed–oxidized single crystal surfaces with flowered LEED patterns absent for annealed surfaces [66]. Most of these studies essentially report multi-domain mixed surface terminations corresponding to out of equilibrium surface configurations. It is, however, well accepted that the stoichiometric surface is not reconstructed and stabilizes through large relaxations.

The determination of the α-Fe_2O_3(0001) surface termination with respect to the oxygen chemical potential is a key experiment to validate the different theoretical approaches [20]. The SXRD experiments were performed at the surface diffraction beamline at ANKA (Karlsruhe, Germany) [31]. A $2+3$ type diffractometer, adapted for surface diffraction experiments under grazing incidence, supports a high-pressure cell (10^{-9} mbar–2 bar) equipped with a furnace (300–1000 K) enabling the use of x-rays through a 2 mm thick 360° beryllium window. This setup enables the *in situ* investigation of a surface under variable p_{O2} and T. The systematic error is estimated to amount to about 10%. A natural hematite single crystal (origin Brazil) with a large (6×15 mm^2) and flat naturally (0001) oriented surface was used. It is believed to correspond to the thermodynamically stable configuration of hematite. The incidence angle was fixed at 0.26° which is the critical angle for total external reflection for the x-rays, α_c, at a photon energy of 9.2 keV. X-ray photoemission spectroscopy (XPS) performed prior to the SXRD investigations revealed that the sample was free from any contaminants other than adsorbed carbon. After the experiment, XPS showed limited Na segregation which fortunately is a very light scatterer compared to Fe (figure 5). Models including Na were found unable to explain the observations.

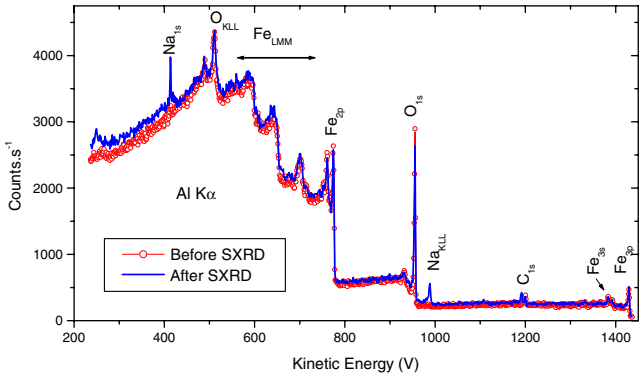

Figure 5. XPS spectra measured on the hematite single crystal prior to and after the SXRD experiment. A monochromatized Al Kα excitation source was used.

Two typical crystal truncation rods (CTRs) of α-Fe_2O_3 (0001) fully characterize the surface: the $(\bar{2}1L)$ CTR has a Bragg peak in the surface plane and is not sensitive to stacking faults whereas the $(10L)$ CTR has only out-of-surface-plane Bragg reflections and is sensitive to stacking faults. By convention we use Bergermayer's [70] notation to describe the surface termination where a subscript number denotes the number of atoms in a layer in the unit cell and the stacking from surface to bulk reads from left to right. Upon reduction from O_3–Fe–Fe to Fe–Fe–O_3 the CTRs show large and characteristic variations in shape [20]. Within a given surface termination and considering the calculated relaxations provided by the theoretical works [19, 23, 70], the resulting rods show relatively small differences only. The different theoretical models [19, 23, 70] predict different stable surface terminations with respect to given chemical oxygen potential and temperature, enabling an experimental discrimination between the proposed theoretical approaches as far as a steady state surface termination can be obtained. The surface was thus

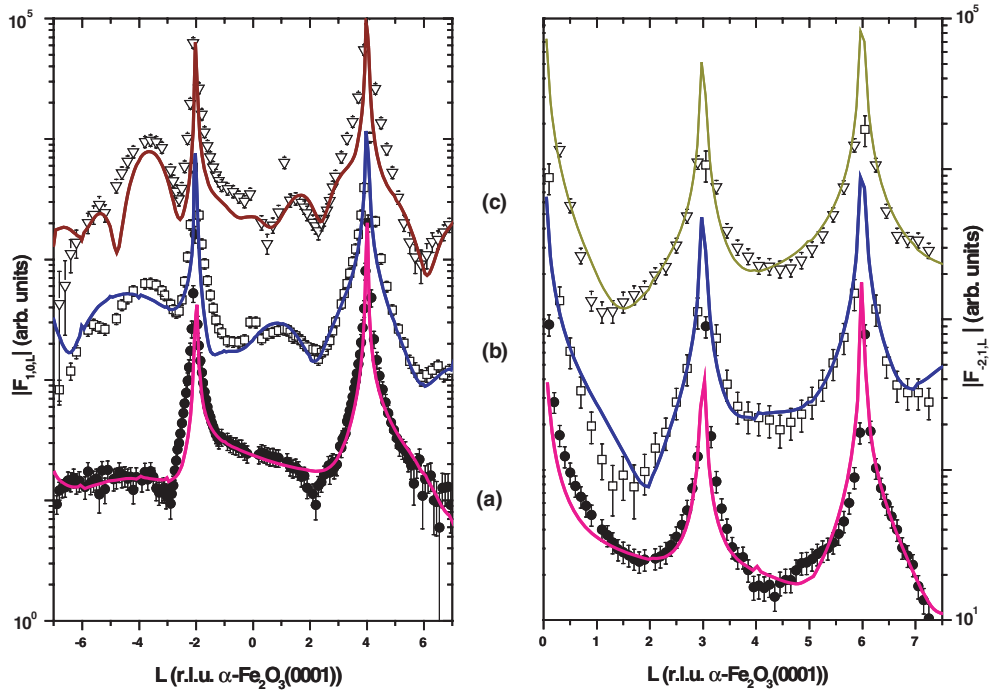

Figure 6. $(10L)$ and $(\bar{2}1L)$ crystal truncation rods of α-$Fe_2O_3(0001)$ for 300 K $< T <$ 850 K and 6×10^{-8} mbar $< p_{O2} <$ 1 bar. The L index describes the perpendicular momentum transfer (in r.l.u. of α-$Fe_2O_3(0001)$). Symbols represent the experimental structure factors. (a) (●) Outgassed surface (1 h, $T = 573$ K, $p_{O2} = 10^{-5}$ mbar); (——) x-ray refined best fit ($\chi^2 \approx 2$) considering a O_3- surface termination; this termination remains stable within -1.1 eV $< \Delta\mu_{O2} < -0.3$ eV. (b) $T = 773$ K with $p_{O2} = 2 \times 10^{-6}$ mbar; (——) best fit ($\chi^2 \approx 3$) considering a O=Fe-surface termination; this termination remains stable within -1.5 eV $< \Delta\mu_{O2} < -0.8$ eV. (c) Annealing at $T = 823$ K (and measurement at 573 K) with $p_{O2} = 1$ bar (▽); (——) best fit ($\chi^2 \approx 4$); (· · · · · ·) best fit considering a O_2–Fe–Fe-surface termination; including 30% of three layer high basal twins. This termination remains stable within -0.8 eV $< \Delta\mu_{O_2} < -0.5$ eV. The systematic error on the structure factor is estimated as ≈10%. The real space models corresponding to the best fits are given in figure 7.

investigated by fast qualitative reciprocal space scans along the L direction and quantitative data obtained through integrated rocking scans (about 150–200 independent structure factors corrected for instrumental factors [73]) were mainly acquired for selected situations where the surface was considered to be in a steady state. During a partial reduction/re-oxidation cycle three steady states could be identified and measured in detail (figure 6).

In order to remove the C surface contamination, the surface was outgassed at $T = 600$ K under $p_{O2} = 10^{-5}$ mbar for 1 h (figure 6(a)). This procedure has been found efficient for air-exposed α-$Fe_2O_3(0001)$ thin films and does not produce any phase change [74]. The overall shape of the rods is consistent with an O_3–Fe–Fe surface termination only. The theoretically proposed O_3–Fe–Fe relaxed surface models reproduce fairly the experimental data in shape with χ^2 values of 4.6, 4.1, 3.8 and 6.6 for the GGA refined models given in references [19, 70, 23] and GGA + U calculations from [23] respectively. The GGA calculations [19, 70] provide the best agreement with the data whereas the GGA + U [23] approach is the worst. A least-square fitting procedure was used to obtain the best agreement to the data. The hematite mesh has high symmetry which strongly limits the possible structural relaxations (figure 4): (i) only two terminations are inequivalent with respect to the O_3 planes; (ii) the threefold axes are lying on the Fe atoms, restricting the possible relaxation of Fe along the c-axis only; (iii) oxygen can move in the surface plane as long as the unit cell keeps its threefold symmetry around the Fe sites, they must in addition remain coplanar. The best fit results (pictured in figure 7) remain close to the GGA models and yield $\delta_1 = -0.30$ Å for a surface with a ∼4 Å rms roughness. A common feature of all theoretical models is a strong inward contraction of the top layers. The present experimental result confirms this trend and shows that these relaxations may indeed be even larger which also may be due to the high temperatures at which the experiments were conducted. The resulting top layer is an almost intermixed Fe_2O_3 layer, thus neutral in charge and without dipole moment.

A second surface configuration, stable over a wide range of p_{O2} is reached by increasing the temperature up to $T =$ 800 K. The model best reproducing the CTR shape is the ferryl-terminated surface, O = Fe-, which has been proposed within GGA and GGA + U models. The best least-square fit to the data is shown in figure 6(b) with $\delta_1 = -0.31$ Å and $\delta_2 = -0.01$ Å along with the perpendicular relaxations reported in figure 7. The predicted GGA outward relaxation is confirmed. Whereas the theoretical models suggest a very narrow stability domain with respect to T and p_{O2}, we observe a quite robust surface termination here which remains compatible with the GGA [70, 23] prediction but out of the $\Delta\mu_{O2}$ range with respect to GGA + U [23]. The extra signal in the $-6 < L < -3$ region of the $(10L)$ CTR increases and takes progressively the shape of a well defined peak. This feature was found

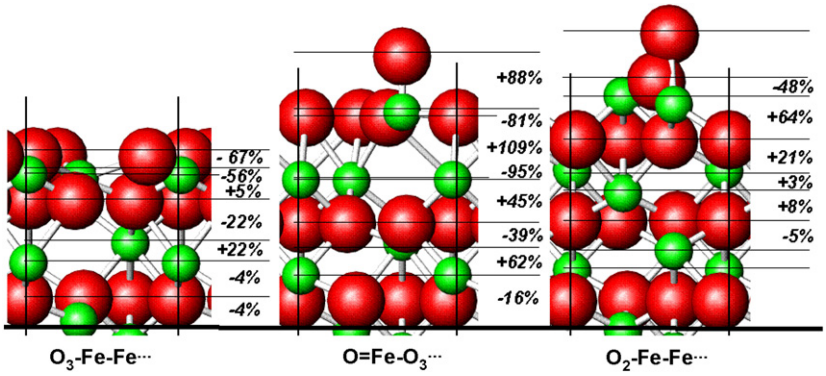

Figure 7. α-Fe_2O_3(0001) stacking for the best fit structures obtained for O_3-, O=Fe- and for O_2–Fe–Fe surface terminations. Large (small) circles stand for O (Fe) atoms.

insensitive to p_{O2}, irreversible and increased systematically with annealing time and T. It is straightforward to reproduce such a feature by including twin domains (the Bragg peak at $L = 4$ appears by symmetry at $L = -4$ for a twin stacking with a width along L related to the number of twinned layers).

The re-oxidation of the surface ($p_{O2} = 1$ bar, $T = 823$ K, figure 6(c)) leads to a O_2–Fe–Fe configuration, as pictured in figure 5. The relaxations are in good agreement with those for a peroxide or dissociated O_2 structure which is predicted as metastable in GGA [70]. The twin signal increases further and narrows. A good fit to the experimental data is obtained by including half a corundum unit cell thick twin islands, covering 30% of the surface.

Finally, the phase stability of the different terminations is in better agreement with the results from DFT–GGA calculations than with those of the DFT–GGA + U approach, though the latter more accurately describes the bulk properties of hematite. This discrepancy likely arises from the correction parameter U for the on-site Coulomb repulsion of the localized Fe 3d electrons, suggesting that this parameter could vary from the bulk to the surface and from one termination to the next.

3.2.2. Thin film growth–oxidation. The single crystal surface studies showed that recovering the most oxidized surface configuration is difficult even at very high oxygen pressures. This fact most likely prevented the growth of hematite thin films using molecular oxygen in usual conditions. However, thin film growth is very desirable for many applications, since thin films may exhibit new properties because of reduced dimensions. Obtaining well ordered single crystalline films of high-structural quality remains a very challenging task for numerous compounds, especially when single crystal surfaces are unavailable. Magnetite layers deposited on Pt surfaces can be transformed into hematite after annealing the layer at 1000 K under high oxygen partial pressures, $p_{O2} = 10^{-1}$ mbar; the resulting layer exhibits a particular surface morphology [75, 76]. Epitaxial hematite thin films can also be directly obtained using extreme oxidizing conditions like NO_2-assisted molecular beam epitaxy (MBE) [77] or atomic oxygen-plasma assisted MBE techniques [78–80]. However, even in highly oxidizing conditions, the early stages of growth are dominated by the occurrence of competing phases like γ-Fe_2O_3(111) which fully transform into α-Fe_2O_3(0001) after a critical thickness of the order of $t = 2$ nm. The nature of the initial phase, as tentatively assigned from reflection high energy electron diffraction (RHEED) patterns (figure 8-left) could be confirmed using various spectroscopy methods [74].

It has been shown that the hematite layers deposited on Pt buffers are of better crystalline quality as compared to the ones deposited directly on sapphire [81]. For example, for a 20 nm thick hematite layer the in-plane mosaic spread reaches 2.3° when sapphire is the substrate as compared to the 0.46° measured on Pt substrates. The main driving force leading to the improved thin film strain release is likely to be the presence of a very well ordered interface dislocation network corresponding to a real space distance of 5 nm (figure 8-right). On the other hand these films are of poor quality compared to the natural bulk crystal that had a mosaic spread as small as 0.01°.

We conclude that, intermediate phases can be observed in the early stages of growth independent of the growth technique or the substrate. These observations show that the interaction of the oxygen gas phase with the hematite surface extends well above the terminal surface plane.

3.2.3. Thin film reduction. Crossing the lower bond of chemical potential necessarily leads to the reduction or decomposition of an oxide material. The way such decomposition occurs remains largely unknown and many questions remain open such as: which are the reduction sub-products?; does surface metallization occur immediately? does the transformation occur at the same oxygen chemical potential when considering a bulk-truncated surface or a thin film?; is such a transformation reversible?

Rock-salt surfaces are poor candidates for such a study since MgO(111) [5] undergoes strong faceting effects due to MgO sublimation and NiO(111) [42] strong metallization effects upon reduction. Since the bulk-truncated hematite surface transformation occurring without reduction already leads to irreversible features due to stacking faults, such investigations appeared more suitable using thin films. We have investigated a 20 nm thick epitaxial α-Fe_2O_3(0001) layer elaborated by atomic oxygen assisted molecular beam epitaxy techniques on a α-Al_2O_3(0001) substrate. The experiments

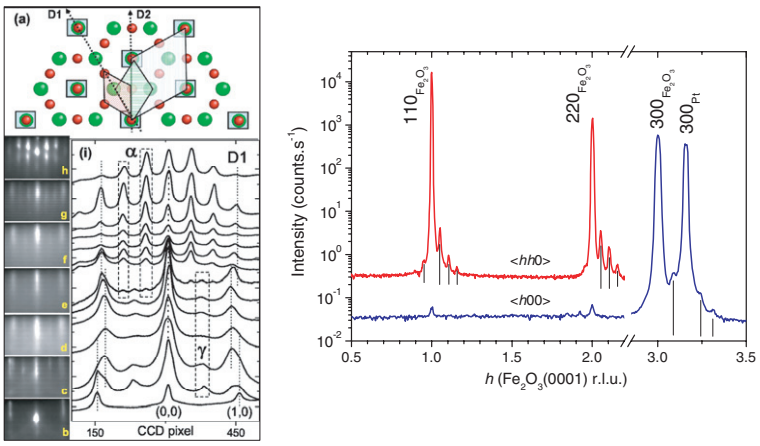

Figure 8. Left: (a) Schematic drawing of superimposed and parameter matched reciprocal lattices of Pt(111) (□), γ-Fe_2O_3(111) (●), and α-Fe_2O_3(0001) (○) assuming cube on cube and $\sqrt{3} \times \sqrt{3}$R30° epitaxial relationships between Pt(111) and γ-Fe_2O_3(111) and α-Fe_2O_3(0001), respectively. The primitive meshes are indicated by patterned areas. (b)–(h) RHEED patterns taken along D1 for $t = 0$, 0.15, 0.3, 0.5, 2, 3.5, and 21 nm. (i) Selected integrated cross sections taken from RHEED patterns oriented along the D1 direction for (from bottom to top) $t = 0$, 0.15, 0.3, 0.5, 1, 2, 3, 4, 5, 9, 12, 18, 20 and 30 nm. Rectangles with dashed line borders indicate peaks relative to the γ- and α-Fe_2O_3 phases only. Right: in-surface-plane reciprocal space scans along the $\langle h00 \rangle$ and $\langle hh0 \rangle$ directions, of a 20 nm thick α-Fe_2O_3(0001)/Pt(111) film. The dislocation satellites are indicated by vertical lines. The experimental data were measured at the critical angle for total external reflection of the x-rays (beamline ID03 (17 keV incident energy) at the ESRF (Grenoble, France)).

were conducted on a dedicated setup located on beamline ID03 at ESRF [32]. A four-circle diffractometer carries a UHV chamber having a 2 mm thick 360° beryllium window equipped with a furnace (up to 1200 K) enabling p_{O2} pressures up to 2 bar. The sapphire substrate peaks were used to index the reciprocal space.

The hematite layer was of single phase with six-fold symmetry and its crystalline quality could be improved through an anneal at 800 K that reduced the in-plane mosaic spread from 2.45° to 0.65° with a domain size of 80 nm. The crystalline quality was poorer as compared to epitaxial layers grown on Pt(111) but without dislocation network; it is thus a more favourable situation as far as the occurrence of new phases is sought.

The hematite surface transforms into magnetite (Fe_3O_4) already at temperatures as low as 657 K which confirms again that outgassing hematite in UHV conditions at lower temperatures does not lead to phase changes. The transformation is found to be progressive: further increase of the temperature increases the relative fraction of magnetite with respect to hematite (see figure 9-top). The phase change was monitored at constant temperature for several hours and found mainly to be limited by kinetic effects. The phenomenon is thus fully out of thermodynamic equilibrium. More interestingly, even starting from a single crystalline hematite layer, magnetite appears in two forms: an epitaxial one that has the same mosaic spread as hematite and a polycrystalline one (that could be evidenced by out of plane mapping of the reciprocal space). Moreover, variable incidence scans showed that the magnetite layer is located close to the surface only.

The Fe_3O_4 layer was then oxidized at 700 K under oxygen pressures ranging from 10^{-7} mbar to 1 bar by steps of a decade of mbar. A large fraction of the layer transforms back to α-Fe_2O_3 below 3 mbar oxygen (see figure 9-bottom). The remaining fraction of the Fe_3O_4 layer transforms into γ-Fe_2O_3,

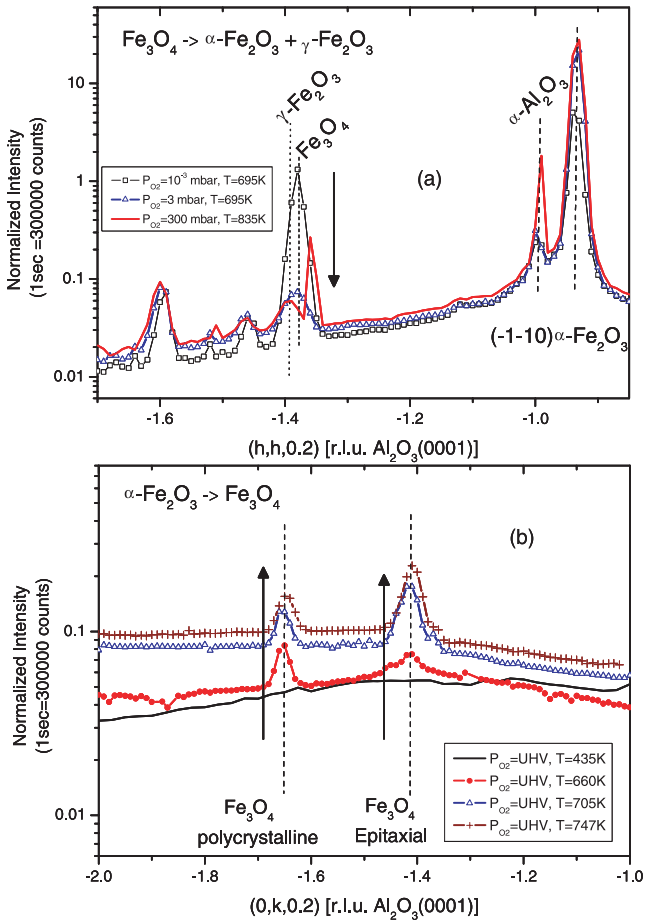

Figure 9. Upperpanel: reduction of α-Fe_2O_3 to Fe_3O_4 as measured by SXRD showing evidence of epitaxial Fe_3O_4 (at (0, −1.4, 0.2)) mixed up with polycrystalline Fe_3O_4 (at (0, −1.6, 0.2)). Lower panel: backward oxidation of Fe_3O_4 embedded in α-Fe_2O_3. After a first oxidation step yielding α-Fe_2O_3 a fraction of the layer transforms into γ-Fe_2O_3.

indicating an irreversible phenomenon. Attempts to fully oxidize this layer into α-Fe_2O_3 up to 1 bar O_2 pressure failed. It is likely that the γ-Fe_2O_3 fraction consists of particles which are known to be stable.

The phase transformation of hematite upon reduction appears thus as a highly complex out of equilibrium process which will require experimental and theoretical efforts before a comprehensive picture can be drawn over a wide range of oxygen chemical potentials.

4. Conclusion

Although apparently very dissimilar in structure and chemical composition, MgO(111), NiO(111) and α-Fe_2O_3(0001) show many features in common. All these crystals are insulators that preferably exhibit polar surfaces made of mixed configurations with relative compositions depending on μ_{O2}. Because of the intrinsic experimental limitations, a satisfying description could only be reached by cross checking experimental and theoretical approaches. In all cases the theoretical description had to take into account μ_{O2} to explain the occurrence and relative stability of the different surface configurations. Similarly, the experiments had to be made in controlled μ_{O2} conditions in order to prevent surface reduction or decomposition.

Another common feature is that all these compounds have very high melting temperatures (T_M(MgO) = 3100 K, T_M(NiO) = 2230 K, T_M(α-Fe_2O_3) = 1840 K) which would lead us to expect high cohesion and relative inertness (if we could extrapolate the way we are thinking about metals and/or semiconductors). Instead, the observed surface configurations show a temperature dependence around room temperature. The polar oriented surfaces appear as highly reactive, even at very low temperature. MgO(111) may be the most extreme case, since atomic mobility within the reconstruction motif is observed at temperatures as low as 140 K. It seems thus not surprising that in early experiments annealing of MgO(111) led to sublimation at comparatively moderate temperatures. Thus, contrarily to many other materials, the cohesion of oxide surfaces strongly depends on μ_{O2}. In other words, we may largely consider these surfaces as in equilibrium with the oxygen gas phase. As a result, the bulk properties of an oxide may only poorly determine its behaviour in UHV conditions. Moreover, the usual surface science recipes consisting of sputter–anneal surface preparations have obviously to be avoided.

At this stage, we still remain far from a complete understanding of the behaviour of these surfaces in real conditions. For example, all these crystals exist in natural conditions with very high quality, which we are not always able to reproduce in controlled laboratory conditions. For instance, the α-Fe_2O_3(0001) natural single crystal has a mosaic spread which is two orders of magnitude smaller than the best epitaxial film we are able to produce along with a much smaller roughness. Much remains also to be done considering the phase changes occurring upon reduction for materials like α-Fe_2O_3(0001), which possess a rich series of reduction sub-products. From the theoretical point of view, puzzling questions also remain open, in particular for strongly correlated oxides. The inclusion of the U potential in the DFT formalism necessary to reproduce bulk parameters has a rather detrimental effect on the prediction of the surface termination with respect to μ_{O2} for α-Fe_2O_3(0001). The structural model obtained for MgO using only DFT ($U = 0$) calculations obviously applies well to NiO(111), indicating also that the U parameter must probably be reduced in the surface region.

Here we have considered explicitly the effect of μ_{O2}, which is an important but only partial constituent of ambient conditions. It appeared, however, to be of major importance with respect to the stability of polar oxide surfaces.

Acknowledgments

We would like to thank all our colleagues who were involved in the work described here and more particularly M Gautier-Soyer, N Jedrecy, N Kasper, H Magnan, and J-B Moussy, who participated in the more recent studies. We are greatly indebted to Herbert Over and to Edvin Lundgren for having invited us to contribute to this special issue.

References

[1] Yamamoto S, Andersson K, Bluhm H, Ketteler G, Starr D E, Schiros T, Ogasawara H, Pettersson L G M, Salmeron M and Nilsson A 2007 *J. Phys. Chem.* C **111** 7848
[2] Hendriksen B L M, Bobaru S C and Frenken J W M 2004 *Surf. Sci.* **552** 229
[3] Ackermann M D, Pedersen T M, Hendriksen B L M, Robach O, Baboru S C, Popa I, Quiros C, Kim H, Hammer B, Ferrer S and Frenken J W M 2005 *Phys. Rev. Lett.* **95** 255505
[4] Giorgio S, Joao S S, Nitsche S, Chaudanson D, Sitja G and Henry C R 2006 *Ultramicroscopy* **106** 503
[5] Henrich V E 1976 *Surf. Sci.* **57** 385
[6] Tasker P W 1979 *J. Phys. C: Solid State Phys.* **12** 4977
[7] Noguera C 2000 *J. Phys.: Condens. Matter* **12** R367
[8] Goniakowski J, Finocchi F and Noguera C 2007 *Rep. Prog. Phys.* at press
[9] Vohs J M and Barteau M A 1986 *Surf. Sci.* **176** 91
[10] Renaud G and Barbier A 2001 *The Chemical Physics of Solid Surfaces* vol 9 (Amsterdam: North-Holland/American Elsevier) p 256
[11] Jedrecy N, Sauvage-Simkin M and Pinchaux R 2000 *Appl. Surf. Sci.* **162/163** 69
[12] Dulub O, Diebold U and Kresse G 2003 *Phys. Rev. Lett.* **90** 016102
[13] Voogt F C, Fujii T, Smulders P J M, Nielsen L, James M A and Hibma T 1999 *Phys. Rev.* B **60** 11193
[14] Chambers S A, Thevuthasan S and Joyce S A 2000 *Surf. Sci.* **450** L273
[15] Pentcheva R, Wendler F, Meyerheim H L, Moritz W, Jedrecy N and Scheffler M 2005 *Phys. Rev. Lett.* **94** 126101
[16] Refson K, Wogelius R A, Fraser D G, Payne M C, Lee M H and Milman V 1995 *Phys. Rev.* B **52** 10823
[17] Finocchi F, Barbier A, Jupille J and Noguera C 2004 *Phys. Rev. Lett.* **92** 136101
[18] Wander A, Schedin F, Steadman P, Norris A, McGrath R, Turner T S, Thornton G and Harrison N M 2001 *Phys. Rev. Lett.* **86** 3811
[19] Wang X G, Weiss W, Shaikhutdinov Sh K, Ritter M, Petersen M, Wagner F, Schlögl R and Scheffler M 1998 *Phys. Rev. Lett.* **81** 1038

[20] Barbier A, Stierle A, Kasper N, Guittet M J and Jupille J 2007 *Phys. Rev.* B **75** 233406
[21] Wang X G, Chaka A and Scheffler M 2000 *Phys. Rev. Lett.* **84** 3650
[22] Wolf D 1992 *Phys. Rev. Lett.* **68** 3315
[23] Rohrbach A, Hafner J and Kresse G 2004 *Phys. Rev.* B **70** 125426
[24] Rollmann G, Rohrbach A, Entel P and Hafner J 2004 *Phys. Rev.* B **69** 165107
[25] Barbier A, Mocuta C, Kuhlenbeck H, Peters K F, Richter B and Renaud G 2000 *Phys. Rev. Lett.* **84** 2897
[26] Stierle A, Renner F, Streitel R, Dosch H, Drube W and Cowie B C 2004 *Science* **303** 1652
[27] Robinson I K and Tweet D J 1992 *Rep. Prog. Phys.* **55** 599
[28] Feidenhans'l R 1989 *Surf. Sci. Rep.* **10** 105
[29] Dosch H 1992 *Springer Tracts in Modern Physics* vol 126 *Critical Phenomena at Surfaces and Interfaces* (Heidelberg: Springer)
[30] Dietrich S and Haase A 1995 *Phys. Rep.* **260** 1
[31] Stierle A, Steinhäuser A, Rühm A, Renner F U, Weigel R, Kasper N and Dosch H 2004 *Rev. Sci. Instrum.* **75** 5302
[32] Bernard P, Peters K, Alvarez J and Ferrer S 1999 *Rev. Sci. Instrum.* **70** 1478
[33] Plass R, Feller J and Gajdardziska-Josifovska M 1998 *Surf. Sci.* **414** 26
[34] Hacquart R and Jupille J 2007 *Chem. Phys. Lett.* **439** 91
[35] Imhoff D, Laurent S, Colliex C and Backhaus-Ricoult M 1999 *Eur. Phys. J. Appl. Phys.* **5** 9
[36] Laurent S, Imhoff D, Colliex C, Hytch M J, Devaud J, Hagege S and Backhaus-Ricoult M 1999 *Mater. Sci. Forum* **294** 325
[37] Backhaus-Ricoult M 2001 *Phil. Mag.* A **81** 1759
[38] Hahn T (ed) 1995 *International Table of Crystallography* (London: Kluwer–Academic)
[39] Cappus D, Xu C, Ehrlich D, Dillmann B, Ventrice V A Jr, Shamery A, Kuhlenbeck H and Freund H J 1993 *Chem. Phys.* **177** 533
[40] Meiklejohn W H 1962 *J. Appl. Phys.* **33** 1328
[41] Soeya S, Nakamura S, Imagawa T and Narishige S 1995 *J. Appl. Phys.* **77** 5838 and references therein
[42] Barbier A and Renaud G 1997 *Surf. Sci.* **392** L15
[43] Erdman N, Warschkow O, Ellis D E and Marks L D 2000 *Surf. Sci.* **470** 1
[44] Plass R, Egan K, Collazo-Davila C, Grozea D, Landree E, Marks L D and Gajdardziska-Josifovska M 1998 *Phys. Rev. Lett.* **81** 4891
[45] Ventrice A, Bertrams T, Hannemann H, Brodde A and Neddermeyer H 1994 *Phys. Rev.* B **49** 5773
[46] Barbier A, Mocuta C, Neubeck W, Mulazzi M, Yakhou F, Chesnel K, Sollier A, Vettier C and de Bergevin F 2004 *Phys. Rev. Lett.* **93** 257208
[47] Barbier A, Mocuta C and Renaud G 2000 *Phys. Rev.* B **62** 16056
[48] Gonze X, Beuken J M, Caracas R, Detraux F, Fuchs M, Rignanese G M, Sindic L, Verstraete M, Zerah G, Jollet F, Torrent M, Roy A, Mikami M, Ghosez Ph, Raty J Y and Allan D C 2002 *Comput. Mater. Sci.* **25** 478–92
[49] Perdew J, Burke R and Enzerhof M 1996 *Phys. Rev. Lett.* **77** 3865
[50] Geneste G, Morillo J and Finocchi F 2002 *Appl. Surf. Sci.* **188** 122
[51] Wander A, Schedin F, Steadman P, Norris A, McGrath R, Turner T S, Thornton G and Harrison N M 2001 *Phys. Rev. Lett.* **86** 3811
[52] Bader R 1991 *Chem. Rev.* **91** 893
[53] Hebenstreit W, Schmid M, Redinger J, Podloucky R and Varga P 2000 *Phys. Rev. Lett.* **85** 5376
[54] Radenović N, Kaminski D, van Enckevort W, Grashwinckel S, Shah I, in't Veld M, Algra R and Vlieg E 2006 *J. Chem. Phys.* **124** 164706
[55] Dinh H T, Kuever J, Mußmann M, Hassel A W, Stratmann M and Widdel F 2004 *Nature* **427** 829–32
[56] Kuiper P, Searle B G, Rudolf P, Tjeng L H and Chen C T 1993 *Phys. Rev. Lett.* **70** 1549
[57] Morrish A H 1994 *Canted Antiferromagnetism: Hematite* (Singapore: World Scientific)
[58] Zang Z and Satpathy S 1991 *Phys. Rev.* B **44** 13319
[59] Kendelewicz T, Liu P, Doyle C, Brown G E, Nelson E J and Chambers S A 1999 *Surf. Sci.* **424** 219
[60] Ivanovskaya M, Kotsikau D, Faglia G, Nelli P and Irkaev S 2003 *Sensors Actuators* B **93** 422
[61] Reddy B V and Khanna S N 2004 *Phys. Rev. Lett.* **93** 068301
[62] Frandsen C and Mørup S 2005 *Phys. Rev. Lett.* **94** 027202
[63] Blake R L, Hessevick R E, Zoltai T and Finger L W 1966 *Am. Mineral.* **51** 123
[64] Condon N G, Murray P W, Leibsle F M, Thornton G, Lennie A R and Vaughan D J 1994 *Surf. Sci. Lett.* **310** L609–13
[65] Condon N G, Leibsle F M, Lennie A R, Murray P W, Parker T M, Vaughan D J and Thornton G 1998 *Surf. Sci.* **397** 278–87
[66] Guo Q, McBreen P H and Møller P J 1999 *Surf. Sci.* **423** 19
[67] Chambers S and Yi S I 1999 *Surf. Sci. Lett.* **439** L785
[68] Ketteler G, Weiss W and Ranke W 2001 *Surf. Rev. Lett.* **8** 661
[69] Lemire C, Bertarione S, Zecchina A, Scarano D, Chaka A, Shaikhutdinov S K and Freund H J 2005 *Phys. Rev. Lett.* **94** 166101
[70] Bergermayer W, Schweiger H and Wimmer E 2004 *Phys. Rev.* B **69** 195409
[71] Shaikhutdinov S K and Weiss W 1999 *Surf. Sci. Lett.* **432** L627
[72] Condon N G, Leibsle F M, Lennie A R, Murray P W, Vaughan D J and Thornton G 1995 *Phys. Rev. Lett.* **75** 1961
[73] Vlieg E 1986 *J. Appl. Crystallogr.* **30** 532
[74] Barbier A, Belkhou R, Ohresser P, Gautier-Soyer M, Bezencenet O, Mulazzi M, Guittet M J and Moussy J B 2005 *Phys. Rev.* B **72** 245423
[75] Weiss W 1997 *Surf. Sci.* **377–379** 943
[76] Weiss W and Ritter M 1999 *Phys. Rev.* B **59** 5201
[77] Fujii T, de Groot F M F, Sawatzky G A, Voogt F C, Hibma T and Okada K 1999 *Phys. Rev.* B **59** 3195
[78] Kim Y J, Gao Y and Chambers S A 1997 *Surf. Sci.* **371** 358
[79] Gao Y and Chambers S A 1997 *J. Cryst. Growth* **174** 446
[80] Gota S, Moussy J B, Henriot M, Guittet M J and Gautier-Soyer M 2001 *Surf. Sci.* **482–485** 809
[81] Barbier A, Bezencenet O, Mocuta C, Moussy J B, Magnan H, Jedrecy N, Guittet M J and Gautier-Soyer M J 2007 *Mater. Sci. Eng.* B **144** 19–22